Research Square

Preprints are preliminary reports that have not undergone peer review.
They should not be considered conclusive, used to inform clinical practice,
or referenced by the media as validated information.

Biosourced choline-functionalized sawdust for dual dye removal: ion-exchange versus multifactorial adsorption mechanisms

Meriem Bendjelloul
University of Relizane
El Hadj Elandaloussi
elhadj.elandaloussi@univ-relizane.dz
University of Relizane
Fatima Zahra Benhachem
University of Tlemcen
Abdelkarim Seghier
University of Relizane
Ahmed Boucherdoud
University of Relizane

Research Article

Keywords: Lignocellulosic waste valorization, Dye adsorption, Ion-exchange mechanism, Multifactorial interactions, Ionic strength resilience, Sustainable wastewater treatment

Posted Date: April 28th, 2026

DOI: https://doi.org/10.21203/rs.3.rs-9451824/v1

License: This work is licensed under a Creative Commons Attribution 4.0 International License.
Read Full License

Additional Declarations: No competing interests reported.

Version of Record: A version of this preprint was published at Chemical Papers on May 23rd, 2026. See the published version at https://doi.org/10.1007/s11696-026-05052-5.

Biosourced choline-functionalized sawdust for dual dye removal: ion-exchange versus multifactorial adsorption mechanisms

Meriem Bendjelloul[1], El Hadj Elandaloussi[*1], Fatima Zahra Benhachem[2], Abdelkarim Seghier[1], Ahmed Boucherdoud[1]

[1]*Environment and Sustainable Development Laboratory, University of Relizane, Bourmadia, 48000 Relizane, Algeria*

[2]*Laboratory of Separation and Purification Technologies, University of Tlemcen, 13000 Tlemcen, Algeria*

[*]Corresponding author, e-mail: elhadj.elandaloussi@univ-relizane.dz

Received [Dates will be filled in by the Editorial office]

Abstract

Choline-functionalized sawdust (CFS) was developed as a sustainable biosorbent for the removal of structurally distinct dyes. Adsorption studies revealed dual mechanistic pathways: Indigo Carmine uptake is dominated by sulfonate–ammonium ion exchange, producing rapid kinetics, and exothermic thermodynamics, whereas Methylene Blue removal proceeds through multifactorial interactions, resulting in slower kinetics, and entropy-driven adsorption. Langmuir isotherms yielded q_{max} values of 125 mg g^{-1} for IC and 43.1 mg g^{-1} for MB, while complementary nonlinear models highlighted the monomechanistic nature of IC adsorption versus the heterogeneous, energetically variable uptake of MB. Adsorption was largely insensitive to ionic strength, underscoring robustness under saline conditions. Regeneration experiments confirmed recyclability, with IC uptake reversed by NaOH and MB restored by NaCl. Overall, CFS emerges as a cost-effective, bio-based adsorbent derived from lignocellulosic waste, combining dual adsorption capacity, ionic strength resilience, and regeneration efficiency, making it a promising candidate for sustainable wastewater treatment.

Keywords: Lignocellulosic waste valorization; Dye adsorption; Ion-exchange mechanism; Multifactorial interactions; Ionic strength resilience; Sustainable wastewater treatment

Introduction

Industrial wastewater contaminated with synthetic dyes represents a critical environmental challenge (Lin et al. 2023; Ardila-Leal et al. 2022; Yaseen et al. 2019). Each year, large quantities of cationic and anionic dyes are discharged into aquatic ecosystems, where their complex aromatic structures confer persistence and resistance to biodegradation (Zhu et al. 2021; Khan et al. 2013). These pollutants impair water quality and light penetration, while posing mutagenic and carcinogenic risks to humans (Singh et al. 2024).

Conventional treatment methods, including coagulation (Rahmoun et al. 2025; Mcyotto et al. 2021), advanced oxidation (Ziembowicz et al. 2025; Heryanto et al. 2025; Martínez Sánchez et al. 2022), and membrane filtration (Wu et al. 2026; Wan et al. 2025), remain costly,

energy-intensive, and prone to generating secondary waste streams (Sheikh et al. 2026; Gavrilaș et al. 2026), highlighting the urgent need for sustainable and low-cost alternatives.

Lignocellulosic biomass has emerged as a promising adsorbent due to its abundance, renewability, and biodegradability (Yadav et al. 2024; Asemave et al. 2021). Sawdust, a ubiquitous by-product of woodworking industries, is particularly attractive for valorization. However, raw sawdust exhibits limited adsorption capacity and poor selectivity, necessitating chemical modification to enhance its performance (Sayed et al. 2024; Tang at al. 2021; Bendjelloul et al. 2021).

Recent advances in polysaccharide chemistry have demonstrated that cationization of cellulose and lignocellulosic derivatives with quaternary ammonium groups can dramatically improve affinity toward anionic pollutants, while maintaining structural integrity and stability (Negi 2025; Toprakçürümez et al. 2025; Acharya et al. 2014). Quaternized cellulose nanofibrils and cationic nanocrystals have shown strong adsorption of anionic dyes, yet most studies focus exclusively on one dye type, leaving a critical gap in understanding dual dye adsorption behavior (Nagendran et al. 2025).

Chemical modification of lignocellulosic substrates has proven essential to overcome the limited adsorption capacity of raw sawdust. Among the different strategies, alkaline pretreatment is widely employed to disrupt lignin–hemicellulose linkages, increase surface area, and expose reactive hydroxyl groups (Demcak et al. 2019; Azzaz et al. 2017; Djilali et al. 2016). This process not only enhances accessibility for subsequent functionalization but also improves the intrinsic affinity of the biomass toward dye molecules. Several studies have demonstrated that alkaline-treated sawdust (ATS) provides a versatile platform for grafting cationic or anionic functionalities, thereby transforming a low-value by-product into a high-performance biosorbent (Ibrahim et al. 2022; Doltabadi et al. 2016; Baouab et al. 2001).

Building on this foundation, quaternary ammonium modification has emerged as a particularly effective route. By introducing permanent positive charges, the cationized ATS can act as a strong anion exchanger, enabling efficient capture of sulfonated dyes such as Indigo Carmine. At the same time, the preserved fibrous structure and stability of cellulose ensure mechanical robustness and reusability. This dual advantage of structural integrity coupled with enhanced electrostatic interactions positions the cationized ATS as an attractive precursor for the development of advanced biosorbents tailored to wastewater treatment.

In this study, alkali-treated sawdust (ATS) was functionalized with choline quaternary ammonium groups to yield a novel biosorbent (CFS). The adsorption performance was systematically investigated for both Indigo Carmine (anionic) and Methylene Blue (cationic),

under varying environmental conditions including pH, ionic strength, and temperature. Regeneration experiments were also conducted to evaluate reusability and stability across multiple cycles. Beyond conventional approaches, adsorption kinetics and equilibrium were modeled using seven nonlinear models, providing a comprehensive evaluation of mechanisms and selectivity. This work establishes choline-functionalized sawdust as a cost-effective and sustainable adsorbent, while offering new insights into dual dye adsorption and advancing the design of biosourced materials for wastewater treatment.

Experimental

Materials

Acetylcholine chloride (≥99%), indigo carmine (≥85%), methylene blue (≥82%), *p*-toluenesulfonyl chloride (≥98%), *p*-toluenesulfonic acid monohydrate (≥98%), pyridine (ACS reagent, 99%), ethanol (92.6-95.2%), sodium chloride (≥99.0%), sodium nitrate (≥99.0%), hydrochloric acid (HCl, ≥37%), and sodium hydroxide (NaOH, ≥98%) were all supplied by Prochima-Sigma (Tlemcen, Algeria) and used as received without further purification. Wood sawdust as received from a local carpenter was thoroughly washed with hot distilled water, then with acetone. The material was dried in an oven at 80 °C until constant weight, and was sieved for a particle size of 250 µm. Stock solutions (1000 mg L^{-1}) were prepared by dissolving indigo carmine and methylene blue in distilled water and test solutions of desired concentrations were obtained by further dilution with distilled water.

Methods

X–ray diffraction (XRD) patterns were recorded from 2θ = 3.5 to 80° on a Phillips X'Pert MPD diffractometer using monochromatic Cu*Kα* radiation (λ = 1.5418 Å) at 40 kV and 30 mA. The Fourier transform infrared (FTIR) spectra were collected using a Nicolet Avatar 330 Fourier transform IR spectrometer. Elemental analysis (CHNS) was performed using a Vario EL III elemental analyzer (Elementar, Germany. The ^{13}C cross polarization magic angle spinning nuclear magnetic resonance (CP/MAS NMR) spectra were recorded on a Bruker 300 (Digital NMR Avance) spectrometer. The morphology of the crosslinked polymer was examined at high magnification using a HITACHI S-4800 SEM. The thermal stability of the samples was performed using TGA on a NETZSCHSTA 409 PC/PG simultaneous thermal analyzer at a heating rate of 10 °C/min under nitrogen atmosphere. The pH_{pzc} of ATS and CFS

was determined using the pH drift (salt addition) method, following the procedure described by Bakatula et al. (2018). Briefly, fixed amounts of adsorbent (0.2 g) were added to 40 mL $NaNO_3$ solutions (0.05 M) previously adjusted to initial pH values ranging from 2 to 12 using 0.1 M HCl or NaOH. The suspensions were agitated for 24 h at room temperature, and the final pH was measured. The pH_{pzc} was identified as the point where the curve of ΔpH ($pH_{final} - pH_{initial}$) versus $pH_{initial}$ crosses zero.

To evaluate the adsorption performance of CFS toward both anionic and cationic dyes, systematic batch experiments were conducted using Indigo Carmine (IC) and Methylene Blue (MB) as model pollutants. Dye concentrations were monitored by UV–Vis spectrophotometry at 610 nm for IC and 663 nm for MB. Aliquots of 25 mL dye solutions were contacted with measured amounts of CFS under magnetic stirring, and the residual concentrations were determined after centrifugation. For IC, a solid-to-solution ratio of 2 $g \cdot L^{-1}$ was applied (50 mg CFS in 25 mL), while for MB the ratio was 3 $g \cdot L^{-1}$ (75 mg CFS in 25 mL). The effect of pH was assessed across the range 2–10. Equilibrium studies were performed over contact times ranging from 10 to 240 min, with IC tested at natural pH and MB at pH = 8, while adsorption isotherms were established by varying the initial dye concentration (IC: 50–1200 $mg \cdot L^{-1}$, MB: 50–500 $mg \cdot L^{-1}$) under optimized equilibrium times. Temperature effects were examined at 25, 35, and 45 °C, and ionic strength was evaluated by adding NaCl (0.1–0.4 M) to the dye solutions. Regeneration and reuse of CFS were tested by saturating the adsorbent with IC or MB, drying at 80 °C, and treating with 1 M NaOH (IC) or NaCl (MB) for 60 min before washing and re-drying. The regenerated material was reused for three consecutive adsorption cycles to assess stability and reusability. Adsorption experiments were performed in triplicate to ensure reproducibility, and the mean values of the three replicates were considered for data analysis. Adsorption capacity and removal efficiency were calculated based on the following mass balance equations:

$$q_e = [(C_i - C_e)/w] \times V \quad (1)$$

$$R(\%) = [(C_i - C_e)/C_i] \times 100 \quad (2)$$

where q_e is the equilibrium adsorption capacity (mg of dye adsorbed per g of adsorbent), R(%) is the removal efficiency expressed as a percentage, C_i is the initial dye concentration ($mg \cdot L^{-1}$), C_e is the equilibrium dye concentration ($mg \cdot L^{-1}$), V is the volume of the solution (L), and w is the mass of adsorbent used (g).

Kinetic modeling was performed using seven nonlinear models (PFO, PSO, Elovich, Avrami, GFO, LFD, and Weber–Morris intraparticle diffusion), while equilibrium adsorption was analyzed using Langmuir, Freundlich, Sips, Temkin, Redlich–Peterson, Toth, and Dubinin–Radushkevich models. All fittings were carried out in OriginPro (OriginLab, USA), and model performance was evaluated according to standard criteria, including root mean square error (RMSE), Akaike information criterion (AIC), and Bayesian information criterion (BIC). The mathematical forms of the applied models are provided in the Supporting Information (Table S2).

Syntheses

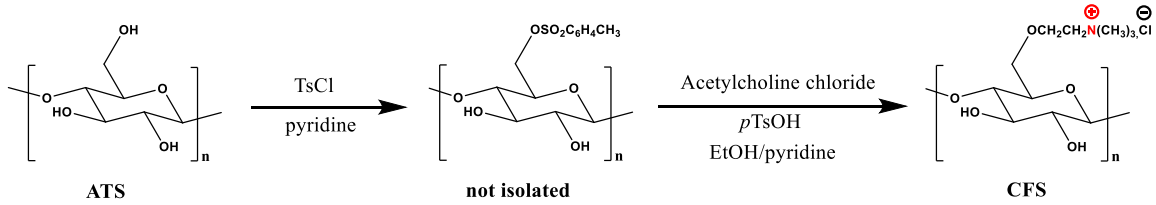
Synthesis of ATS

ATS was synthesized by alkaline treatment of wood sawdust. In a 1 L Erlenmeyer flask, 50 g of sawdust was added to 500 mL of 20 wt% NaOH solution and stirred for 4 h. The suspension was filtered, and the solid was thoroughly washed with distilled water until neutral pH. The material was then impregnated overnight with 500 mL of 1 N HCl solution, filtered, and washed again with distilled water until neutral pH, followed by acetone rinsing. The resulting ATS was air-dried, sieved through a 250 µm mesh, and obtained as 27 g of a yellowish solid.

Synthesis of CFS

Several preliminary attempts to quaternize ATS, including direct reaction with chlorocholine chloride or with choline chloride on isolated tosylated ATS, were unsuccessful. The successful strategy consisted of a sequential two-step process: ATS was first tosylated in pyridine with *p*-toluenesulfonyl chloride (Reactor 1), while choline chloride was prepared in parallel by saponification of acetylcholine chloride in ethanol/pyridine with *p*-toluenesulfonic acid (Reactor 2). The solution from Reactor 2 was then added dropwise to Reactor 1, and the combined mixture was heated at 60 °C for 2 h to afford the quaternized product (CFS). The synthetic pathway leading to CFS is illustrated in Scheme 1. Specifically, 17 g (89.16 mmol) of p-toluenesulfonyl chloride was dissolved in 200 mL pyridine at 0 °C, and 15 g of ATS was added gradually in small portions. After addition, the mixture was heated at 60 °C for 2 h and then allowed to return to room temperature. In parallel, choline chloride was prepared by saponification of acetylcholine chloride: 20.16 g (111 mmol) of acetylcholine chloride was dissolved in 60 mL of a mixture of ethanol and pyridine (1:2 v/v), treated with 2.12 g of *p*-toluenesulfonic acid, and stirred for 1 h. This solution was added dropwise to the suspension

of tosylated ATS, and the mixture was further heated at 60 °C for 2 h. After cooling, the suspension was filtered, and the solid was thoroughly washed with distilled water until no chloride ions were detected by $AgNO_3$ test, followed by acetone rinsing. The product was oven-dried at 80 °C to yield 18.23 g of CFS as a dark brown solid.



Scheme 1 Synthetic route leading to the choline-functionalized sawdust (CFS). The process involves tosylation of the alkali-treated sawdust (ATS), and subsequent quaternization with choline chloride.

Results and discussion

Characterization of CFS sorbent

The determination of the point of zero charge (pH_{pzc}) provided clear evidence of the distinct surface properties of the two materials. ATS exhibited a pH_{pzc} of 5.38, which is consistent with values reported for untreated or alkaline-treated sawdust, typically 5.2–5.6 (Bajpai et al. 2012). In contrast, CFS showed a significantly lower pHpzc of 3.2, in line with literature on cellulose modified with quaternary ammonium groups (Echeverría et al. 2024). This shift reflects the introduction of permanent positive charges on the surface, confirming the successful functionalization of sawdust with choline groups. These values, determined by the drift method (Bakatula et al. 2018), are presented in Fig. S1.

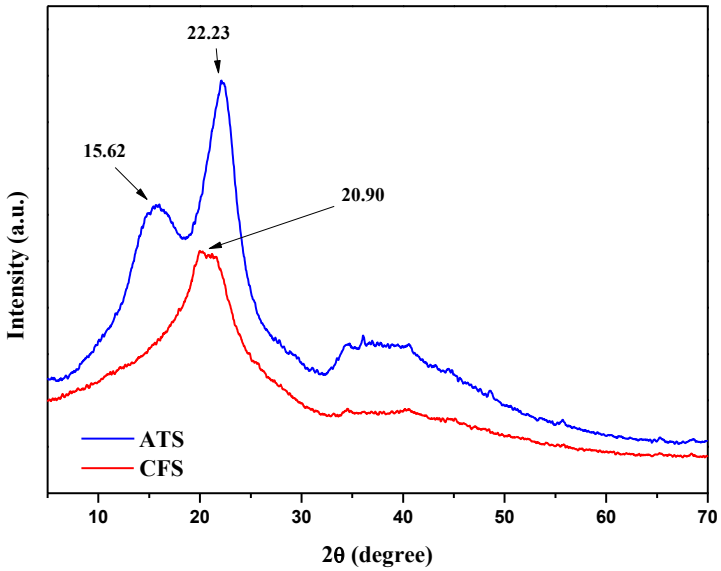


Fig. 1. X-ray diffraction patterns of alkali-treated sawdust (ATS) and choline-functionalized sawdust (CFS).

In line with the surface charge results, XRD analysis confirmed the structural differences between ATS and CFS. As shown in Fig. 1, ATS exhibited sharp peaks at 2θ = 15.62° and 22.23°, characteristic of cellulose I crystalline domains (Park et al. 2010). In contrast, CFS displayed a broadened peak centered at 2θ = 20.90°, indicating reduced crystallinity as a result of chemical functionalization with choline groups, consistent with previous reports on modified cellulose systems (Stanciu et al. 2025). FTIR spectra (Fig. 2) provided further evidence of structural modifications between ATS and CFS. The spectrum of ATS displayed characteristic cellulose absorption bands, including O–H stretching (~3418 cm^{-1}), C–H stretching (~2911 cm^{-1}), and C–O–C vibrations (~1052 cm^{-1}). The absence of the C=O band (~1730 cm^{-1}) indicates that alkaline treatment removed a significant portion of lignin. Additional bands at 1059 and 1020 cm^{-1} correspond to C–O–C and C–O–H stretching vibrations of the sugar ring, while the peak at 892 cm^{-1} is associated with glycosidic bonds in the cellulose backbone. In contrast, functionalization with choline induced slight peak shifts (red or blue shifts) due to rearrangements in the cellulose chain. CFS exhibited additional absorption bands at 1595 cm^{-1}, 1497 cm^{-1} and ~949 cm^{-1}, assigned to quaternary ammonium groups ($C–N^+$ stretching). These features are consistent with previous reports (Huang et al., 2025) and provide clear evidence of successful choline grafting. A slight shoulder at 1743 cm^{-1} was also observed in the CFS spectrum, absent in ATS, which may reflect residual carbonyl vibrations associated with structural rearrangements during functionalization. CHNS elemental analysis reinforced the FTIR evidence, validating the presence of functional groups introduced

during modification. ATS exhibited no detectable nitrogen, whereas CFS contained 1.12% nitrogen, confirming the incorporation of quaternary ammonium groups. The carbon content increased from 44.05% to 48.82%, consistent with the introduction of organic moieties, while the hydrogen content decreased from 6.89% to 5.85%.

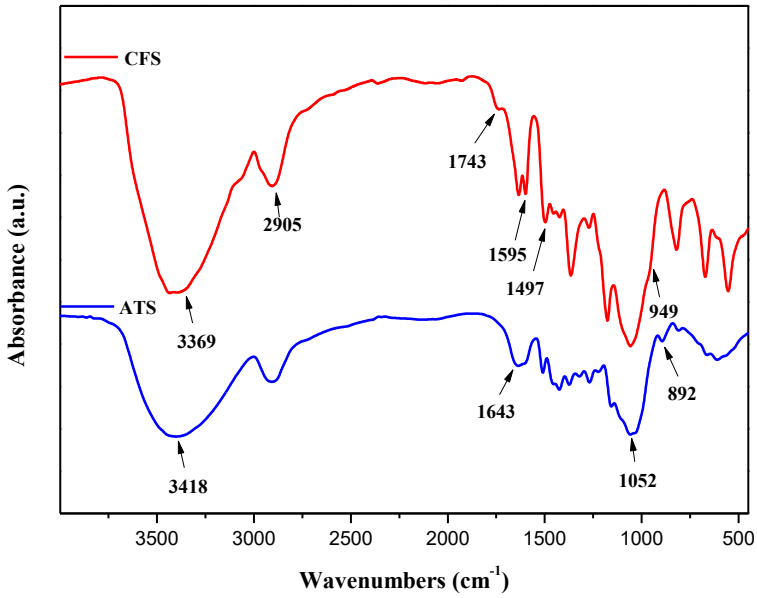


Fig. 2. FTIR spectra of ATS and CFS.

As shown in Fig. 3, solid-state ^{13}C NMR spectra provided further evidence of successful functionalization. ATS exhibited typical cellulose resonances between 60–105 ppm, corresponding to C2, C3, and C5 carbons, and a signal at ~89 ppm assigned to crystalline C4. The alkaline treatment of raw sawdust removes hemicelluloses, lignin, and extractives, thereby enriching the cellulose fraction and generating a negatively charged surface. This was consistent with the attenuation of aromatic and carbonyl signals in the ^{13}C CP/MAS spectrum. The subsequent acidification step reconverts residual –ONa groups into –OH, stabilizing the cellulose matrix and preventing interference during subsequent functionalization. The resulting ATS thus exhibits a cleaner spectral profile. In contrast, CFS showed an additional broad resonance centered at 56.5 ppm, attributable to the five carbons of the $–CH_3–CH_2–N^+(CH_3)_3$ moiety of choline. This new signal, absent in ATS, confirmed the incorporation of quaternary ammonium groups, in agreement with elemental analysis and FTIR results, and consistent with previously reported quaternary ammonium cellulose derivatives (Toprakçürümez et al. 2025; Ali et al. 2023). The degree of quaternization (DQ) was estimated from solid-state ^{13}C NMR by integrating the relative intensities of the choline carbons (56.5 ppm) against the C1 resonance of cellulose (~106 ppm), which appears as a distinct singlet and thus provides a reliable internal

reference. This calculation yielded a DQ value of 0.69, higher than the estimation from CHNS elemental analysis (1.12% N, DQ = 0.24), explicitly assuming that CFS consists exclusively of cellulose units. The discrepancy between the two methods can be explained by the semi-quantitative nature of CP/MAS NMR and the partial overlap of choline resonances with C6 of ATS and residual lignin carbons. Nevertheless, both approaches consistently confirm the successful incorporation of quaternary ammonium groups.

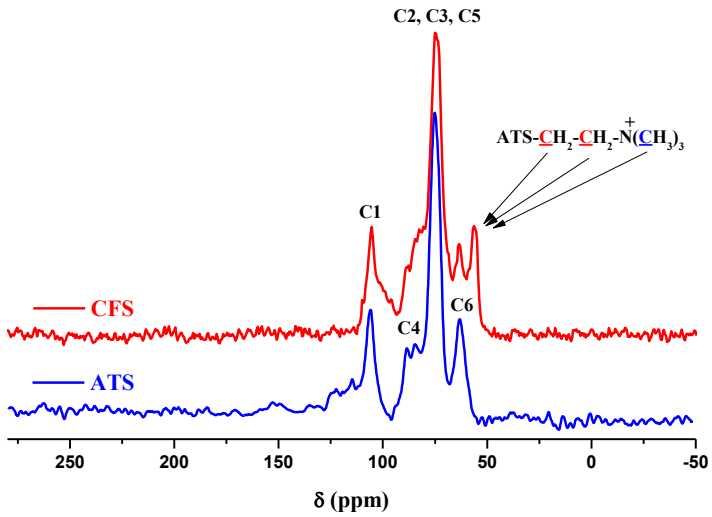


Fig. 3. Solid-state ^{13}C CP/MAS NMR spectra of ATS and CFS.

In addition to the structural evidence provided by solid-state ^{13}C NMR, thermogravimetric (TGA) and derivative (dTG) analyses revealed clear differences in the thermal behavior of ATS and CFS. As shown in Fig. 4, ATS exhibited a major weight loss between 250–480 °C, with a sharp dTG peak at ~333 °C corresponding to cellulose degradation and a second peak at ~485 °C due to char combustion, consistent with the pyrolysis behavior of lignocellulosic components (Yang et al. 2007). In contrast, CFS displayed an additional weight loss around 200–250 °C, with a distinct dTG peak at ~226 °C assigned to the decomposition of quaternary ammonium groups. The main cellulose degradation shifted slightly to ~338 °C, and the final decomposition occurred at higher temperature (~534 °C), evidencing enhanced thermal stability upon functionalization. These changes indicate that the incorporation of quaternary ammonium groups not only modifies the chemical structure but also alters the thermal degradation pathway of cellulose, consistent with previous studies on modified cellulose derivatives (Echeverría et al. 2024). Moreover, the DSC curves provide complementary information to TGA/dTG by confirming the energetic nature of the thermal events (Fig. S2). For ATS, two major exothermic peaks are observed: the first around ~428 °C,

corresponding to cellulose pyrolysis, and the second near ~600 °C, associated with the oxidation and combustion of char residues. In contrast, CFS exhibits an additional exothermic event at ~243 °C, assigned to the decomposition of quaternary ammonium groups, followed by the main cellulose degradation (~400 °C) and a more intense exothermic peak between ~600–700 °C, reflecting the combustion of functionalized carbonaceous residues. These DSC results corroborate the TGA/dTG findings: the functionalization introduces a distinct decomposition step and enhances the overall thermal stability, while also altering the degradation pathway of cellulose.

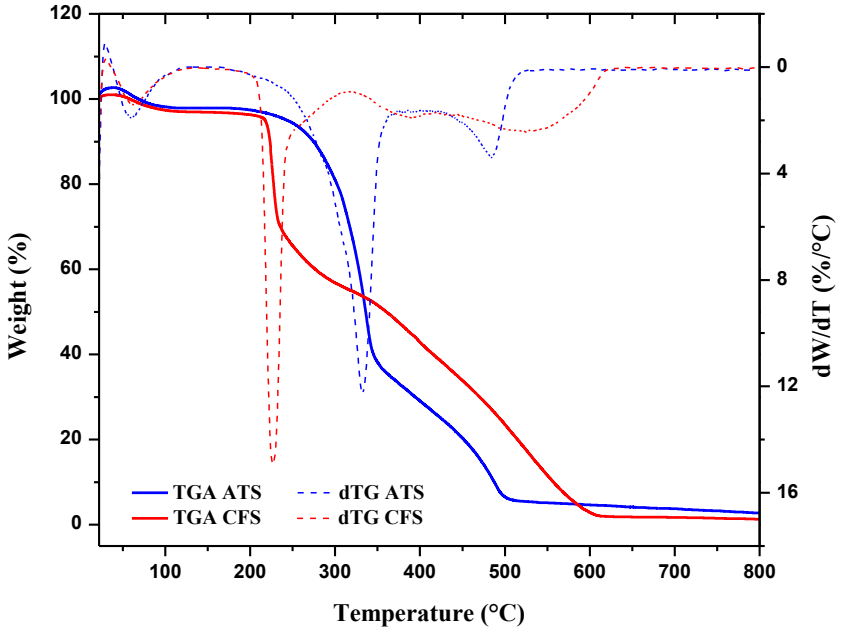


Fig. 4. Thermogravimetric (TGA) and derivative (dTG) curves of ATS and CFS.

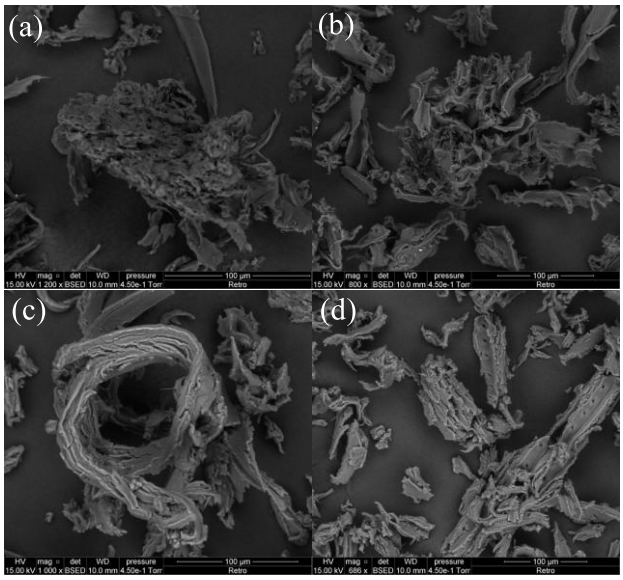


Fig. 5. SEM micrographs of ATS (a, b) and CFS (c, d).

Fig. 5 presents SEM micrographs highlighting the morphological differences between ATS and choline-functionalized sawdust (CFS). ATS displays a relatively smooth fibrillar surface typical of lignocellulosic substrates, whereas CFS exhibits a rougher and more irregular texture. Although the microstructural details are not sharply resolved, these changes indicate disruption of the cellulose matrix upon functionalization, consistent with the structural modifications evidenced by XRD, FTIR, and NMR analyses.

Effect of pH

The effect of pH on dye adsorption revealed contrasting behaviors between IC and MB. Sorption efficiency of IC remained nearly constant (~99.9%) across the pH range tested (2–10), indicating that its uptake is largely independent of solution pH and dominated by strong ion-exchange interactions (Fig. 6). In contrast, MB exhibited a progressive increase in sorption efficiency, rising from 71% at pH 2 to a maximum of 94% at pH 8, before slightly decreasing at pH 10. This trend reflects the influence of protonation on adsorption site availability, with optimal performance under mildly basic conditions. Considering the point of zero charge (pH_{pzc} = 3.2) of CFS, the surface is positively charged below this value and negatively charged above it. IC, as an anionic dye, maintained nearly constant removal efficiency due to the presence of quaternary ammonium groups that remain permanently positively charged, thereby overriding the effect of the pH_{pzc}. Conversely, MB, a cationic dye, exhibited lower adsorption at pH < 3.2 due to electrostatic repulsion, and higher adsorption at pH > 3.2 due to electrostatic attraction, with maximum efficiency at pH 8. The slight decrease at pH 10 may be attributed to competition with hydroxyl ions or site saturation.

Mechanistically, IC adsorption onto CFS is dominated by ion exchange between the sulfonate groups of IC and the permanently charged quaternary ammonium groups of CFS. This explains the nearly constant removal efficiency across all pH values, as the ion exchange mechanism overrides the effect of the pH_{pzc}. Secondary contributions from hydrogen bonding may occur, but ion exchange remains the primary driving force. In contrast, MB adsorption involves a synergistic mechanism. Electrostatic interactions modulated by the pHpzc play a central role, complemented by hydrogen bonding with hydroxyl groups and dispersion forces. At highly alkaline pH, competition with hydroxyl ions may reduce adsorption efficiency. Importantly, spectroscopic analyses confirm that only a small fraction of lignin remains after

alkaline treatment; nevertheless, these residual aromatic structures may still contribute to MB adsorption through π–π stacking with the dye's aromatic rings. Although secondary in nature, this mechanism enhances binding affinity and complements electrostatic attraction, hydrogen bonding, van der Waals, and hydrophobic interactions, thereby stabilizing MB within the porous matrix of CFS.

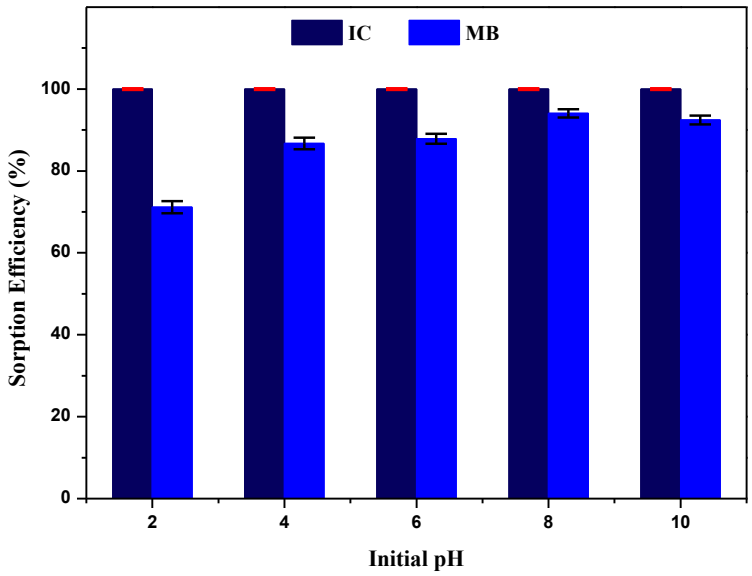


Fig. 6. Influence of initial pH (2–10) on the removal efficiency of IC and MB by CFS. Adsorption was performed using 50 mg of biosorbent for IC and 75 mg for MB in 25 mL of 25 mg·L^{-1} solution, stirred for 2 h.

Adsorption kinetics

As shown in Fig. 7, the adsorption kinetics revealed a sharp contrast between IC and MB. Within the first 10 min of contact, IC removal reached 84%, whereas MB removal was only 51%. This rapid uptake of IC is consistent with a dominant ion-exchange mechanism between the sulfonate groups of the dye and the quaternary ammonium sites of CFS, leading to fast saturation of available binding sites. In contrast, MB adsorption proceeded more slowly, requiring ~280 min to reach equilibrium ($q_e \approx 7.25$ mg g^{-1}) compared to ~160 min for IC ($q_e \approx 7.99$ mg g^{-1}). The slower kinetics of MB reflect a multi-step process involving electrostatic attraction, hydrogen bonding, π–π stacking with residual lignin domains, and van der Waals interactions, which collectively delay the attainment of equilibrium.

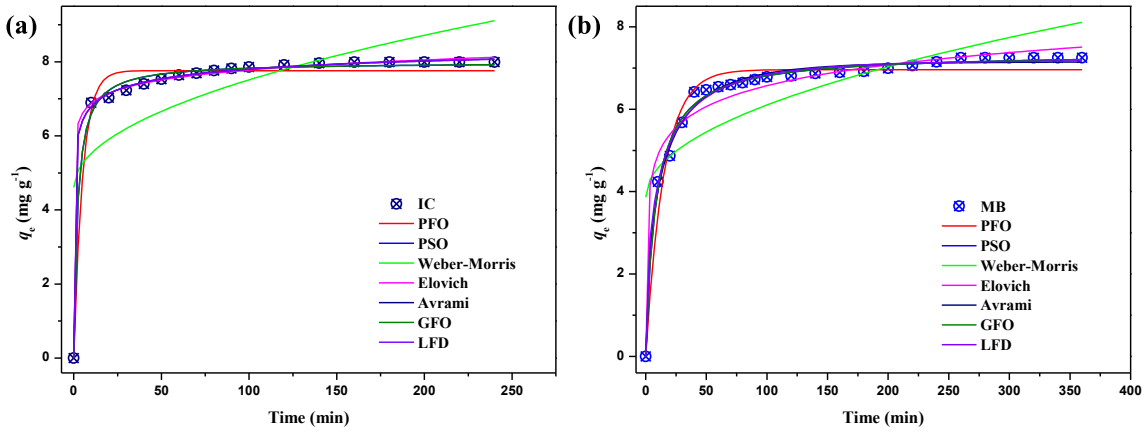


Fig. 7. Nonlinear kinetic modeling of IC and MB adsorption onto CFS. Conditions: IC at natural pH with 50 mg biosorbent in 25 mL of 25 mg·L^{-1} solution; MB at pH 8 with 75 mg biosorbent in 25 mL of 25 mg·L^{-1} solution. Experiments were conducted at ambient temperature, with aliquots withdrawn up to 240 min (IC) and 360 min (MB). Data were fitted to pseudo-first-order, pseudo-second-order, intraparticle diffusion, Elovich, Avrami, GFO, and LFD models.

The adsorption kinetics of Indigo Carmine (IC) and Methylene Blue (MB) onto the CFS biosorbent were systematically investigated using multiple nonlinear models. For IC, the PFO model proved inadequate, underestimating the equilibrium capacity and yielding relatively poor statistics (adj $R^2 = 0.979$). In contrast, the PSO model provided an excellent fit (adj $R^2 = 0.995$, RMSE = 0.12), strongly supporting a chemisorption mechanism dominated by ion exchange between the sulfonate groups of IC and the quaternary ammonium sites of CFS. This observation is consistent with previous reports on cellulose-based adsorbents, where PSO kinetics have been shown to adequately describe the adsorption of dyes and other organic pollutants (Toprakçürümez et al. 2025; Saad & Mahmoud, 2025; Hubbe et al., 2019). The Elovich and Avrami models reinforced this interpretation; in particular, the Avrami exponent ($n \approx 0.19$) revealed an extremely rapid initial uptake followed by stabilization, consistent with the quasi-instantaneous nature of ion exchange. The GFO model further confirmed an effective order close to two, corroborating the PSO findings. Finally, the generalized LFD model (adj $R^2 = 0.999$, $\alpha \approx 0.19$) demonstrated that although external film diffusion contributes to the process, it is not the rate-limiting step. Taken together, these results indicate that IC adsorption is essentially monomechanistic, governed by rapid ion exchange, with diffusion playing only a secondary role.

In contrast, MB exhibited a more complex kinetic behavior. The PFO model failed to capture the process adequately (adj $R^2 = 0.964$), excluding a simple first-order mechanism. Conversely, the PSO model achieved excellent agreement (adj $R^2 = 0.993$, RMSE = 0.12), suggesting that chemisorption contributes significantly. This outcome is consistent with recent studies on hyper-crosslinked cellulose adsorbents, where PSO kinetics have been shown to reliably capture the uptake of pharmaceuticals despite the coexistence of multiple adsorption pathways (Benosmane et al., 2021). However, the Avrami exponent ($n \approx 0.54$) pointed to a more gradual adsorption pathway, indicative of multiple concurrent mechanisms. The Elovich model, although less accurate (adj $R^2 = 0.968$), confirmed the heterogeneity of the adsorption surface. The GFO model again yielded an effective order close to two, reinforcing the PSO interpretation. Importantly, the generalized LFD model (adj $R^2 = 0.991$, $\alpha \approx 0.54$) highlighted the stronger role of diffusion in MB uptake compared to IC. Mechanistically, this is consistent with the cationic and aromatic nature of MB: its adsorption involves electrostatic attraction favored by the pHpzc of CFS, hydrogen bonding with surface hydroxyl groups, π–π stacking with residual lignin structures preserved after alkaline treatment, and van der Waals interactions. At highly alkaline pH, competition with hydroxyl ions may reduce adsorption efficiency.

Overall, IC adsorption onto CFS is characterized by rapid kinetics and essentially controlled by a near-monomechanistic pathway, as evidenced by the superior fits of PSO, Avrami, and LFD, and by the very low α value that minimizes the role of diffusion. By contrast, MB uptake is slower and inherently more complex, requiring complementary models to capture its heterogeneous and diffusion-influenced behavior. The higher α value in the LFD model emphasizes the importance of diffusion in MB uptake. This comparative framework underscores the preferential affinity of CFS for anionic dyes, while highlighting the multifaceted nature of cationic dye adsorption.

Table 1. Kinetic parameters obtained from nonlinear fitting of seven adsorption models (PFO, PSO, Weber–Morris, Elovich, Avrami, General Fractional Order (GFO) and generalized Liquid Film Diffusion (LFD)) for IC and MB adsorption onto the CFS biosorbent.

Model	**Parameters**	**Pollutant**	
		IC (±SE)	**MB** (±SE)
	$q_{e,exp}$ (mg g^{-1})	**7.99**	**7.25**
PFO	$q_{e,cal}$ (mg g^{-1})	7.76	6.96

	k_1 (min^{-1})	0.199	0.067
	R^2_{adj}	0.979	0.964
	RMSE [AIC ; BIC]	0.25 [–44.95 ; –43.17]	0.28 [–57.21 ; –54.86]
PSO	$q_{e,cal}$ (mg·g^{-1})	7.99	7.37
	k_2 (g mg^{-1} min^{-1})	0.059	0.016
	R^2_{adj}	0.995	0.993
	RMSE [AIC ; BIC]	0.12 [–69.69 ; –67.91]	0.12 [–95.28 ; –92.92]
ID	k_{id} (mg g^{-1}·min$^{-1/2}$)	0.29	0.22
	C (mg g^{-1})	4.61	3.86
	R^2_{adj}	0.417	0.555
	RMSE [AIC ; BIC]	1.32 [14.22 ; 15.99]	0.99 [3.55 ; 5.91]
Elovich	α (mg g^{-1} min^{-1})	1.79×10^6	58.53
	β (g mg^{-1})	2.57	1.36
	R^2_{adj}	0.998	0.968
	RMSE [AIC ; BIC]	0.06 [–93.41 ; –91.63]	0.26 [–59.56 ; –57.21]
Avrami	$q_{e,cal}$ (mg·g^{-1})	8.57	7.19
	n	0.186	0.537
	k_{av} (min^{-n})	1.024	0.254
	R^2_{adj}	0.999	0.996
	RMSE [AIC ; BIC]	0.05 [–97.72 ; –95.04]	0.13 [–91.36 ; –87.83]
GFO	$q_{e,cal}$ (mg·g^{-1})	7.99	7.37
	k_f (min^{-1})	0.475	0.122
	n	2.00	2.00
	R^2_{adj}	0.994	0.992
	RMSE [AIC ; BIC]	0.12 [–67.69 ; –65.02]	0.12 [–93.28 ; –89.74]
LFD	$q_{e,cal}$ (mg·g^{-1})	8.57	7.19
	k_f (min$^{-\alpha}$)	1.024	0.253
	α	0.186	0.537
	R^2_{adj}	0.999	0.991
	RMSE [AIC ; BIC]	0.25 [–44.94 ; –43.16]	0.28 [–57.21 ; –54.86]

Adsorption isotherms

The equilibrium isotherms revealed a markedly higher adsorption capacity for IC (114 mg·g^{-1}) compared to MB (36 mg·g^{-1}). As shown in Fig. 8a, IC exhibited a steep initial uptake and nearly quantitative removal, consistent with a dominant ion exchange mechanism. In contrast, MB showed a more gradual increase and lower saturation capacity, reflecting a synergistic adsorption process involving mixed interactions (Fig. 8b).

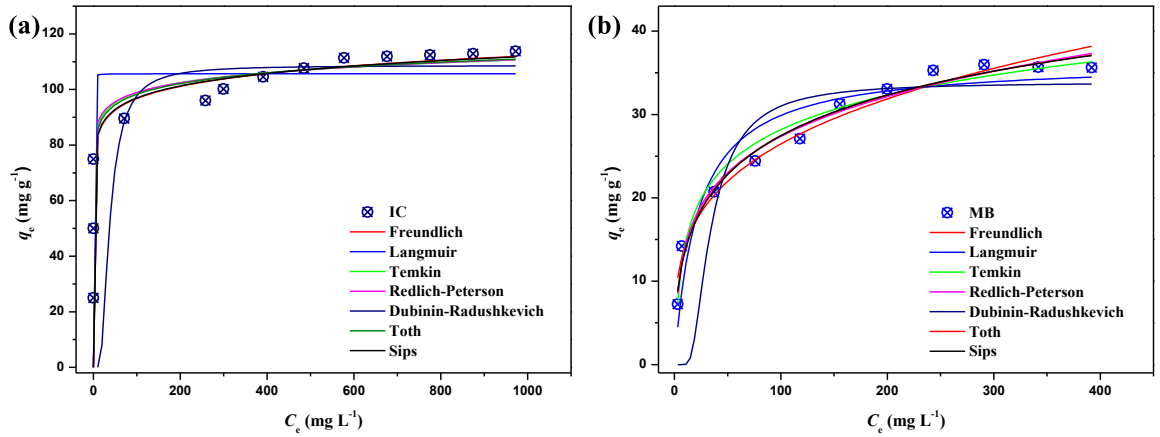


Fig. 8. Isotherm modeling of Indigo Carmine (IC) and Methylene Blue (MB) adsorption onto CFS. Experimental data were fitted to Freundlich, Langmuir, Sips, Temkin, Redlich–Peterson, Toth, and Dubinin–Radushkevich models. Conditions: IC adsorption at natural pH with 50 mg biosorbent in 25 mL solutions (50–1200 mg L^{-1}), MB adsorption at pH 8 with 75 mg biosorbent in 25 mL solutions (50–500 mg L^{-1}), stirred for 120 min at ambient temperature.

The equilibrium adsorption of Indigo Carmine (IC) and Methylene Blue (MB) onto CFS was analyzed using multiple nonlinear models. This comparative evaluation highlights the distinct mechanistic pathways governing the uptake of the two dyes (Fig. 8; Table 2). For IC, the Freundlich, Temkin, and Redlich–Peterson models provided the most reliable fits (adj $R^2 \approx$ 0.885–0.889), whereas Langmuir showed weaker agreement (adj R^2 = 0.840) and Dubinin–Radushkevich failed entirely. The very low Freundlich exponent ($n \approx 0.064$) indicates strong heterogeneity and highly favorable adsorption at low concentrations. Temkin analysis confirmed a progressive decrease in adsorption energy with coverage, consistent with electrostatic repulsion as exchange sites become saturated. Redlich–Peterson, with $g \approx 0.95$, approached Langmuir behavior but retained heterogeneity. These results align with the ion exchange nature of IC adsorption through highly favorable sulfonate–ammonium interactions, with diffusion playing only a secondary role.

Table 2. Nonlinear isotherm parameters for IC and MB adsorption onto CFS biosorbent. IC was best described by Freundlich, Temkin, and Redlich–Peterson models, highlighting strong ion-exchange control and heterogeneity at low concentrations. MB fitted better to Redlich–Peterson, Toth, Temkin, and Sips models, confirming a heterogeneous and multifactorial adsorption pathway with significant diffusion contributions.

Model	Pollutant

	Parameter	IC	MB
Langmuir	q_{max} (mg g^{-1})	105.65	36.39
	K_L (L/mg)	27.88	0.046
	R^2_{adj}	0.839	0.904
	RMSE [AIC ; BIC]	10.14 [64.25 ; 65.38]	2.73 [27.67 ; 26.96]
Freundlich	K_F	72.07	7.69
	n	0.064	0.268
	R^2_{adj}	0.889	0.969
	RMSE [AIC ; BIC]	8.43 [59.44 ; 60.57]	1.55 [13.73 ; 14.52]
Sips	q_{max} (mg g^{-1})	966.22	64.02
	K_S (L/mg)	2.39×10^{-16}	0.005
	n	0.07	0.442
	R^2_{adj}	0.877	0.976
	RMSE [AIC ; BIC]	8.45 [64.17 ; 63.20]	1.27 [14.73 ; 12.50]
Temkin	b_T (mg/g)	5.19	5.96
	K_T (L/mg)	1.84×10^{6}	1.128
	R^2_{adj}	0.885	0.975
	RMSE [AIC ; BIC]	8.51 [64.48 ; 63.53]	1.40 [11.46 ; 12.25]
Redlich–Peterson	K_{RP}	9870.16	7.35
	a_{RP}	125.2	0.677
	β	0.950	0.790
	R^2_{adj}	0.885	0.977
	RMSE [AIC ; BIC]	8.19 [63.34 ; 62.37]	1.26 [11.14 ; 12.33]
Toth	q_{max} (mg g^{-1})	333.51	98.47
	K_T (L/mg)	8.94×10^{23}	1.455
	t	0.047	0.223
	R^2_{adj}	0.874	0.976
	RMSE [AIC ; BIC]	8.56 [64.51 ; 63.53]	1.27 [14.69 ; 12.46]
Dubinin–Radushkevich	q_{max} (mg g^{-1})	108.60	33.84
	K_{DR}	1.73×10^{-4}	1.44×10^{-4}
	R^2_{adj}	–0.185	0.658
	RMSE [AIC ; BIC]	26.32 [90.23 ; 90.16]	5.43 [41.24 ; 42.04]

In contrast, MB adsorption was best described by Redlich–Peterson (adj R^2 = 0.977), Toth (adj R^2 = 0.977), and Temkin (adj R^2 = 0.975), while Freundlich also performed well (adj R^2 = 0.969). Langmuir was less adequate (adj R^2 = 0.904), and Dubinin–Radushkevich again failed. The Freundlich exponent ($n \approx 0.27$) reflects surface heterogeneity and favorable adsorption at low concentrations. Temkin analysis revealed a linear decline in adsorption energy, consistent with electrostatic repulsion as MB accumulates. Redlich–Peterson, with $g \approx 0.79$, confirmed intermediate behavior between Langmuir and Freundlich, while the Toth model, despite its statistical strength, suffered from unstable parameters. Mechanistically, MB

adsorption is multifactorial: electrostatic attraction (favored by the pH_{pzc} of CFS), hydrogen bonding with surface hydroxyl groups, π–π stacking with residual lignin, and both external and intraparticle diffusion contribute significantly.

Taken together, equilibrium modeling highlights a clear divergence between IC and MB adsorption on CFS. IC uptake is best captured by heterogeneous models such as Freundlich, Temkin, and Redlich–Peterson, reflecting strong affinity at low concentrations and a gradual decrease in adsorption energy with site saturation. MB, by contrast, requires models that incorporate energetic variability and diffusion contributions, consistent with its slower and more complex binding. These complementary outcomes corroborate the kinetic findings and emphasize the dual functionality of CFS: a highly efficient adsorbent for anionic dyes like IC, while also capable of accommodating more heterogeneous interactions in the case of cationic MB.

To further consolidate the equilibrium analysis, the Sips model reinforced the divergence between IC and MB adsorption on CFS. For IC, the poor statistical fit and unstable parameters confirm that its uptake is best described by simpler, near-monomechanistic models. In contrast, MB adsorption was well captured by Sips (adj $R^2 = 0.977$), with realistic parameters ($q_{max} \approx 64$ mg·g^{-1}, $n \approx 0.44$). The exponent $n < 1$ reflects surface heterogeneity and a distribution of adsorption energies, consistent with the multifactorial nature of MB uptake. This outcome corroborates the Redlich–Peterson and Temkin analyses, situating MB adsorption in an intermediate regime between homogeneous and heterogeneous binding.

Table 3. Langmuir maximum adsorption capacities (q_{max}, mg g^{-1}) of Indigo Carmine (IC) and Methylene Blue (MB) on CFS compared with representative adsorbents from the literature (25 °C).

Adsorbent	Dye	q_{max} (mg g^{-1})	t (h); [pH]	Ref
CFS	IC	105.65	2; [Nat. pH]	This study
Carbon nanotubes	IC	78.65	2.5; [6]	(Elamin et al. 2023)
Commercial AC	IC	79.5	1.5; [2]	(Harrache et al. 2019)
AC from sawdust	IC	55.8	3; [2]	(Bhowmik et al. 2021)
Rice husk ash	IC	29.3	8; [5.4]	(Lakshmi et al. 2009
Banana peel	IC	56.18	2; [3]	(Channei et al. 2021)
Acetate sawdust	IC	142.85	1; [6]	(Bendjelloul et al. 2021)
CFS	MB	36.39	2; [8]	This study
Magnetic chitosan–biochar	MB	113.15	3; [6]	(Wang et al. 2024)

Sawdust	MB	30.12	1; [7]	(Abyar et al. 2025)
Chitosan crosslinked composite	MB	323.26	24; [–]	(Liu et al. 2022)

When expressed in molar terms, the maximum adsorption capacity of IC reached 0.227 mmol·g^{-1} (0.454 meq·g^{-1} considering its divalent charge), whereas MB attained only 0.114 mmol·g^{-1} (0.114 meq·g^{-1}). Elemental analysis (1.12 % N, ~0.8 mmol N·g^{-1}) indicates that IC uptake corresponds to ~28 % of the available quaternary ammonium sites, consistent with dual sulfonate anchoring and efficient charge neutralization. By contrast, MB mobilized only ~14 % of these sites, reflecting its reliance on weaker, multifactorial interactions involving hydroxyl groups of the cellulose backbone and residual lignin domains. Importantly, despite its larger molecular dimensions (~1.4–1.6 nm vs. ~0.8–1.0 nm for MB), IC achieved higher uptake and charge neutralization, underscoring the specificity and strength of sulfonate–ammonium ion exchange. This quantitative comparison highlights the robust ion exchange pathway for IC versus the more heterogeneous binding landscape of MB.

Table 3 compares the Langmuir maximum adsorption capacities (q_{max}) of CFS with representative adsorbents reported in the literature. For Indigo Carmine (IC), CFS exhibited a q_{max} of 105.65 mg g^{-1} at natural pH, which is higher than values obtained with carbon nanotubes and commercial activated carbon, and markedly superior to rice husk ash. Only acetate-functionalized sawdust showed a higher capacity (142.85 mg g^{-1}). For Methylene Blue (MB), CFS reached 36.39 mg g^{-1}, comparable to raw sawdust (30.12 mg g^{-1}) but lower than magnetic chitosan-composite biochar and chitosan crosslinked composites. These results highlight the strong affinity of CFS for anionic dyes such as IC, while MB adsorption remains moderate due to its multi-step mechanism and competition effects.

Effect of Ionic Strength on Adsorption of IC and MB onto CFS

The influence of ionic strength was evaluated by introducing NaCl (0–0.4 M) into the adsorption system (Fig. 9). The results highlight a clear mechanistic distinction between IC and MB uptake on CFS. For Indigo Carmine (IC), removal efficiency remained nearly complete, decreasing only slightly from 99.9% to 99.3% as NaCl concentration increased. This limited inhibition demonstrates the robustness of the ion-exchange mechanism, in which sulfonate groups of IC interact strongly with quaternary ammonium sites on CFS. Although Na^+ ions compete for exchange sites, the affinity of IC remains dominant, confirming that IC adsorption is largely salt-resistant. By comparison, Methylene Blue (MB) exhibited greater sensitivity to ionic strength. Removal efficiency decreased more noticeably, from 99.9% to 95.4% over the

same NaCl range. While the absolute reduction still leaves high removal efficiency, it reflects the vulnerability of MB adsorption to charge screening. MB uptake relies on electrostatic attraction, π–π stacking, and hydrogen bonding, all of which are weakened when Na^+ ions shield the negative charges on the CFS surface. This effect highlights the secondary nature of MB adsorption relative to the robust ion-exchange mechanism governing IC.

In summary, the ionic strength study highlights the contrasting resilience of IC and MB adsorption on CFS. IC removal remained virtually unaffected even at high NaCl concentrations, confirming the stability of its binding pathway. MB, although still efficiently removed, showed a measurable decline under saline conditions, reflecting the greater vulnerability of its adsorption forces to charge screening. Similar trends have been reported for MB adsorption on macro fungi and others biosorbents, where increased ionic strength reduces uptake due to competition and shielding effects (Maurya et al., 2006; Al-Samman and Sánchez, 2022). This comparative outcome emphasizes the operational selectivity of CFS: highly robust toward anionic dyes such as IC, while moderately sensitive in the case of cationic MB, making it particularly promising for effluent treatment under saline conditions.

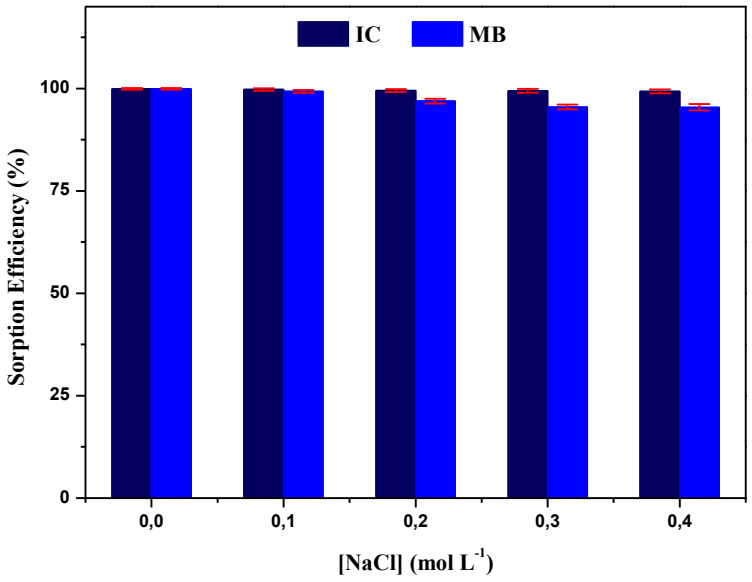


Fig. 9. Removal efficiency of IC and MB by CFS in NaCl matrices at ionic strengths ranging from 0 to 0.4 M. Conditions: IC at natural pH with 50 mg biosorbent in 25 mL of 50 $mg \cdot L^{-1}$ solution; MB at pH 8 with 75 mg biosorbent in 25 mL of 50 $mg \cdot L^{-1}$ solution. Experiments were stirred for 120 min at ambient temperature.

Thermodynamic Analysis

Thermodynamic parameters were evaluated to assess the influence of temperature (298–318 K) on the adsorption of MB and IC onto CFS. Values derived from Van't Hoff plots (Fig S3) are summarized in Table S1. Thermodynamic parameters were determined using the Van't Hoff equation:

$$\ln(K_c) = -\frac{\Delta H^\circ}{RT} + \frac{\Delta S^\circ}{R} \quad (3)$$

with $K_c = q_e/C_e$.

The Gibbs free energy was calculated as:

$$\Delta G^\circ = \Delta H^\circ - T\Delta S^\circ \quad (4)$$

where ΔH° is enthalpy change (kJ·mol^{-1}), ΔS° is entropy change (J·mol^{-1}·K^{-1}), and ΔG° is Gibbs free energy (kJ·mol^{-1}).

For MB, the adsorption process is endothermic (ΔH^0 = +68.3 kJ/mol) and entropy driven (ΔS^0 = +279.85 J/mol·K), which indicates increased randomness at the solid–liquid interface. The negative Gibbs free energy values (ΔG^0 = –17.85 to –20.65 kJ/mol) confirm that adsorption is spontaneous and becomes more favorable with rising temperature. The modest increase in q_e supports this thermodynamic trend, suggesting that higher thermal energy facilitates dye diffusion and strengthens adsorbent–adsorbate interactions. Comparable behavior has been documented for methylene blue adsorption onto rejected tea leaves, where uptake improved with rising temperature (Nasuha et al. 2010). Conversely, Indigo Carmine (IC) exhibits an exothermic adsorption profile (ΔH^0 = –54.74 kJ/mol) with a negative entropy change (ΔS^0 = –63.71 J/mol·K), which indicates a more ordered system upon adsorption. The highly negative ΔG^0 values (–35.75 to –34.48 kJ/mol) confirm strong spontaneity across all temperatures, but the slight decrease in q_e suggests that elevated temperatures marginally hinder IC uptake. This behavior is consistent with ion-exchange mechanisms, which are typically exothermic and less favored at higher temperatures due to reduced electrostatic interactions. Similar trends have been reported in ion-exchange adsorption studies, where negative entropy and enthalpy values reflect ordering at the solid–liquid interface and diminished uptake with increasing temperature (Toprakçürümez et al. 2025).

Regeneration and Reuse of CFS

The regeneration and reuse experiments demonstrate the robustness and economic viability of the synthesized CFS material. The reusability of choline-functionalized sawdust

(CFS) was evaluated over three consecutive adsorption–desorption cycles (Fig. 10). The removal efficiency of IC reached 99.97% during the first adsorption cycle, confirming the strong affinity of CFS for anionic dyes. Regeneration with 1 M NaOH solution resulted in nearly complete desorption, and subsequent reuse maintained high removal efficiencies. After three cycles, IC elimination remained close to 99%, indicating that the ion-exchange mechanism is fully reversible and that the structural integrity of CFS is preserved. This stability highlights the suitability of CFS for repeated use in effluent treatment without loss of performance. Methylene Blue (MB) was regenerated using 1 M NaCl solution, which effectively displaced the cationic dye from the adsorbent surface. The first reuse cycle showed only a minor decrease (≈0.6%) in sorption capacity, and subsequent cycles maintained nearly constant removal efficiency. This confirms that MB adsorption, although multifactorial, can be reversed efficiently by ionic competition with Na^+, allowing full recovery of the adsorbent.

Considered jointly, the regeneration studies demonstrate that CFS can be reused multiple times without significant loss of adsorption capacity for either IC or MB. The choice of regenerant reflects the mechanistic differences: NaOH is optimal for desorbing anionic dyes through ion-exchange reversal, while NaCl is effective for cationic dye desorption via charge displacement. These findings emphasize the practical applicability of CFS as a resource-efficient, recyclable adsorbent for dye removal in real effluent treatment scenarios. The regeneration cycles further confirm the robustness of CFS for both dye classes. Thermodynamic analysis suggests that MB adsorption is predominantly governed by hydrogen bonding and dipolar interactions, complemented by van der Waals forces, which explains its efficient reversibility under ionic competition. While this study focused on three cycles, the structural stability of the lignocellulosic framework indicates that extended reuse is feasible.

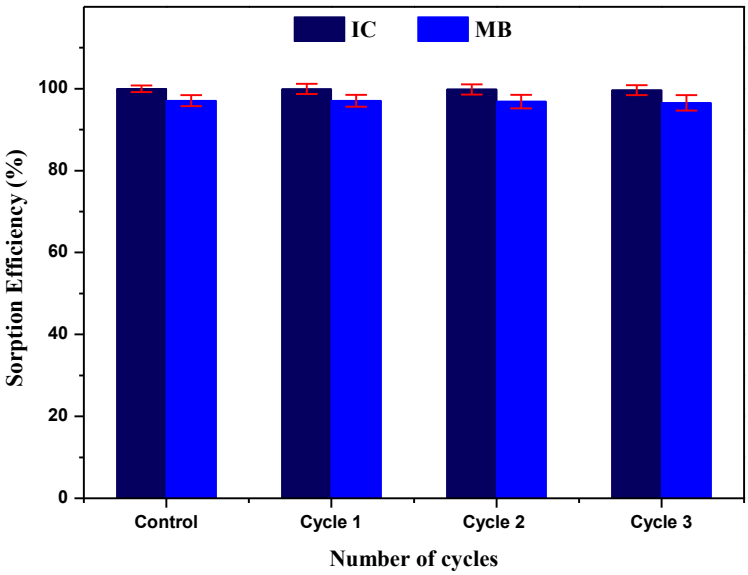


Fig 10. Sorption efficiency of IC and MB over successive usage cycles. Regeneration and reuse were assessed over three cycles. Each cycle consisted of sorption under the working conditions, desorption with 20 mL of 1 M NaOH (for IC) and 1 M NaCl (for MB) for 120 min, followed by rinsing with distilled water, drying overnight at 80 °C, and reuse in the subsequent cycle.

Adsorption Mechanism

The mechanistic evaluation highlights distinct pathways for IC and MB uptake on CFS. As for Indigo Carmine (IC), adsorption is dominated by sulfonate–ammonium ion exchange. This mechanism is supported by its high affinity, resilience to ionic strength, and exothermic thermodynamic profile with negative entropy change, reflecting ordering at the solid–liquid interface. Kinetic modeling fits a pseudo-second-order equation consistent with chemisorption, while regeneration with NaOH confirms the reversibility of the exchange process. As it can be seen in Fig. S4, FTIR spectra further substantiate this pathway, showing shifts in quaternary ammonium C–N^+ stretching bands and disappearance of lignin carbonyl shoulders, direct evidence of sulfonate–ammonium interactions. SEM image (Fig. 11a) reveals compact, homogeneous coverage, consistent with strong anchoring. For Methylene Blue (MB), adsorption proceeds via multifactorial interactions. Electrostatic attraction to negatively charged sites is complemented by π–π stacking with aromatic moieties and hydrogen bonding with hydroxyl groups. This explains its sensitivity to ionic strength, endothermic and entropy-driven thermodynamics, and efficient regeneration with NaCl through charge displacement. FTIR spectra show reduced O–H band intensity (~3420 cm^{-1}) and shifts in aromatic C=C and carbonyl regions, confirming involvement of hydroxyl and aromatic groups. SEM micrograph (Fig. 11b) displays fibrous, irregular textures with localized clusters,

consistent with weaker, heterogeneous binding. FTIR and SEM analyses, though modest, provide widely accepted evidence for adsorption mechanisms. Band shifts and intensity changes in FTIR spectra, together with surface morphology modifications observed by SEM, are consistent with dye–adsorbent interactions reported in similar biosorbent systems (Belin Jude et al., 2025; Kuppusamy et al., 2026).

The adsorption pathways illustrated in the graphical abstract are corroborated by kinetic, thermodynamic, FTIR, and SEM analyses. While the abstract provides a schematic overview, this section presents the spectroscopic and morphological evidence that substantiates these mechanisms. Collectively, the results highlight the dual functionality of CFS: a robust ion-exchange process governing the uptake of anionic dyes such as IC, and a set of versatile multifactorial interactions enabling the efficient capture of cationic dyes such as MB

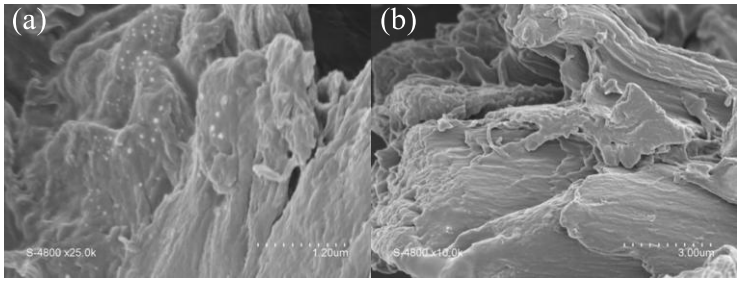


Fig. 11. SEM micrographs of CFS surface morphology before and after dye adsorption. (a) IC uptake produced compact and homogeneous coverage, consistent with strong ion-exchange anchoring. (b) MB adsorption yielded fibrous, irregular textures with localized clusters, reflecting weaker multifactorial interactions and incomplete site saturation.

Conclusions

This work establishes choline-functionalized sawdust (CFS) as a sustainable and efficient adsorbent for structurally distinct dyes. Comprehensive characterization confirmed successful functionalization and the presence of versatile binding sites. Adsorption studies revealed a dual mechanistic behavior: Indigo Carmine removal is governed by sulfonate–ammonium ion exchange, producing compact surface coverage, rapid kinetics, and exothermic thermodynamics, whereas Methylene Blue uptake proceeds through multifactorial interactions (electrostatic attraction, hydrogen bonding, π–π stacking, dipolar and van der Waals forces), resulting in slower kinetics, and entropy-driven adsorption. FTIR and SEM analyses, though modest, provided consistent evidence of these mechanistic differences, highlighting dense IC

anchoring versus superficial MB coverage. Importantly, adsorption performance was largely insensitive to ionic strength variations, underscoring the robustness of CFS under saline conditions. Regeneration experiments further validated the recyclability of the material: IC removal was efficiently reversed with NaOH through ion-exchange displacement, while MB uptake was restored with NaCl via charge competition. Beyond mechanistic insights, this study demonstrates the potential of CFS as a cost-effective, bio-based material derived from lignocellulosic waste, contributing to circular economy strategies and sustainable wastewater treatment. The dual adsorption capacity, combined with resilience to ionic strength and effective regeneration, consolidates CFS as a promising candidate for practical dye removal and environmental remediation.

References

Abyar H, Nowrouzi M, Rezaei H (2025) Efficient and Eco-Friendly Sawdust Adsorbent for Methylene Blue Removal: Adsorption Optimization, Kinetics, and Isotherm Modelling. Int J Environ Res 19:128. https://doi.org/10.1007/s41742-025-00790-y

Acharya S, Abidi N, Rajbhandari R, et al. (2014) Chemical cationization of cotton fabric for improved dye uptake. Cellulose 21:4693–4706. https://doi.org/10.1007/s10570-014-0457-2

Ali A, Ganie SA, Mir TA et al. (2023) Synthesis, characterization and disinfection efficiency evaluation of quaternary ammonium iodide derivatives of gum arabic. J Polym Environ 31:4210–4222. http://doi.org/10.1007/s10924-023-02874-2

Al-Samman MT, Sánchez J (2022) Chitosan- and Alginate-Based Hydrogels for the Adsorption of Anionic and Cationic Dyes from Water. Polymers 14:1498. https://doi.org/10.3390/polym14081498

Ardila-Leal LD, Poutou-Piñales RA, Pedroza-Rodríguez AM, Quevedo-Hidalgo BE (2021) A brief history of colour, the environmental impact of synthetic dyes and removal by using laccases. Molecules 26:3813. https://doi.org/10.3390/molecules26133813

Asemave K, Thaddeus L, Tarhemba PT (2021) Lignocellulosic-based sorbents: a review. Sustain Chem 2:271–285. https://doi.org/10.3390/suschem2020016

Azzaz AA, Jellali S, Souissi R, et al. (2017) Alkaline-treated sawdust as an effective material for cationic dye removal from textile effluents under dynamic conditions: breakthrough curve prediction and mechanism exploration. Environ Sci Pollut Res 24:18240–18256. https://doi.org/10.1007/s11356-017-9388-4

Bajpai S, Bajpai M, Rai N (2012) Sorptive removal of ciprofloxacin hydrochloride from simulated wastewater using sawdust: Kinetic study and effect of pH. Water SA 38(5):673–682. http://doi.org/10.4314/wsa.v38i5.4

631 Bakatula EN, Richard D, Neculita CM, Zagury GJ (2018) Determination of point of zero charge
632 of natural organic materials. Environ Sci Pollut Res 25:7823–7833.
633 https://doi.org/10.1007/s11356-017-1115-7

634 Baouab MHV, Gauthier R, Gauthier H, El Baker Rammah M (2001) Cationized sawdust as ion
635 exchanger for anionic residual dyes. J Appl Polym Sci 82:31–37.
636 https://doi.org/10.1002/app.1820

637 Belin Jude A, Divya P, Chaitanya M et al. (2025) Comparative Adsorption of Synthetic Dyes
638 Using Low-Cost Biosorbents: Analysis of Thermodynamics and Isotherms. Glob NEST
639 J 27: 1-11. https://doi.org/10.30955/gnj.06897

640 Bendjelloul M, Elandaloussi EH, de Menorval LC (2021) Sodium acetate functionalized timber
641 sawdust for effective removal of cadmium ions and basic/acid dyes from aqueous
642 solutions. Desalin Water Treat 233:158–169. https://doi.org/10.5004/dwt.2021.27594

643 Benosmane S, Bendjelloul M, Elandaloussi, EH et al. (2021) Experimental and modeling study
644 on adsorption of emerging contaminants onto hyper-crosslinked cellulose. Chem Pap
645 75:4021–4034. https://doi.org/10.1007/s11696-021-01637-4

646 Bhowmik S, Chakraborty V, Das P (2021) Batch adsorption of indigo carmine on activated
647 carbon prepared from sawdust: A comparative study and optimization of operating
648 conditions using response surface methodology. Res Surf Interfaces 3:100011.
649 https://doi.org/10.1016/j.rsurfi.2021.100011.

650 Channei D, Jannoey P (2021) Adsorption of indigo carmine dye onto porous adsorbent derived
651 from banaba peels waste. TiS 18:9. https://doi.org/10.48048/tis.2021.9

652 Demcak S, Balintova M, Demcakova M, Csach K, Zinicovscaia I, Yushin N, Frontasyeva M
653 (2019) Effect of alkaline treatment of wooden sawdust for the removal of heavy metals
654 from aquatic environments. Desalin Water Treat 155:207–215.
655 https://doi.org/10.5004/dwt.2019.24053

656 Djilali A, Elandaloussi EH, Aziz A, de Ménorval LC (2016) Alkaline treatment of timber
657 sawdust: a straightforward route toward effective low-cost adsorbent for the enhanced
658 removal of basic dyes from aqueous solutions. J Saudi Chem Soc 20 (Suppl 1):S241–
659 S249. https://doi.org/10.1016/j.jscs.2012.10.013

660 Doltabadi M, Alidadi H, Davoudi M (2016) Comparative study of cationic and anionic dye
661 removal from aqueous solutions using sawdust-based adsorbent. Environ Prog Sustain
662 Energy 35:1078–1090. https://doi.org/10.1002/ep.12334

663 Echeverría C, Arnaldos-Pérez I, Barranco R et al. (2024) Synthesis and characterization of
664 cellulose derivatives for enhanced antimicrobial activity. Cellulose 31:1729–1740.
665 http://doi.org/10.1007/s10570-023-05655-1

666 Elamin MR, Abdulkhair BY, Elzupir AO (2023) Removal of ciprofloxacin and indigo carmine
667 from water by carbon nanotubes fabricated from a low-cost precursor: Solution
668 parameters and recyclability. Ain Shams Eng J 14:101844.
669 https://doi.org/10.1016/j.asej.2022.101844

Gavrilaș S, Gerőcs T, Chereji BD, Munteanu FD (2026) Trends in advanced wastewater treatment technologies: from membrane bioreactors to advanced oxidation processes. Water 18:350. https://doi.org/10.3390/w18030350

Harrache Z, Abbas M, Aksil T, Trari M (2019) Thermodynamic and kinetics studies on adsorption of Indigo Carmine from aqueous solution by activated carbon. Microchem J 144:180–189. https://doi.org/10.1016/j.microc.2018.09.004

Heryanto H, Tahir D (2025) Trends, mechanisms, and the role of advanced oxidation processes in mitigating azo, triarylmethane, and anthraquinone dye pollution: a bibliometric analysis. Inorg Chem Commun 175:114104. https://doi.org/10.1016/j.inoche.2025.114104

Huang X, Ganie SA, Rather LJ et al. (2025) Synthesis, characterization, and biological activity assessment of quaternary ammonium-functionalized cellulose: enhanced antimicrobial features, free radical scavenging and thermal stability. Cellulose 32:5935–5957. http://doi.org/10.1007/s10570-025-06601-z

Hubbe MA, Azizian S, Douven S (2019) Implications of apparent pseudo-second-order adsorption kinetics onto cellulosic materials: A review. BioRes 14:7582–7626. https://doi.org/10.15376/biores.14.3.7582-7626

Ibrahim NA, Abdellatif FHH, Hasanin MS, Abdellatif MM (2022) Fabrication, characterization, and potential application of modified sawdust sorbents for efficient removal of heavy metal ions and anionic dye from aqueous solutions. J Clean Prod 332:130021. https://doi.org/10.1016/j.jclepro.2021.130021

Khan R, Bhawana P, Fulekar MH (2013) Microbial decolorization and degradation of synthetic dyes: a review. Rev Environ Sci Biotechnol 12:75–97. https://doi.org/10.1007/s11157-012-9287-6

Kuppusamy B, Mohamed Ismail FR, Balakrishnan P et al. (2026) From Biomass to Adsorbent: A Comprehensive Review on Bio-Derived Carbons for Dye Removal. Polymers 18:180. https://doi.org/10.3390/polym18020180

Lakshmi UR, Srivastava VC, Mall ID, Lataye DH (2009) Rice husk ash as an effective adsorbent: Evaluation of adsorptive characteristics for Indigo Carmine dye. J Environ Manag 90:710–720. https://doi.org/10.1016/j.jenvman.2008.01.002

Lin J, Ye W, Xie M, et al. (2023) Environmental impacts and remediation of dye-containing wastewater. Nat Rev Earth Environ 4:785–803. https://doi.org/10.1038/s43017-023-00489-8

Liu XJ, Li MF, Ma JF, Bian J, Peng F (2022) Chitosan crosslinked composite based on corncob lignin biochar to adsorb methylene blue: Kinetics, isotherm, and thermodynamics. Colloids Surf A Physicochem Eng Asp 642:128621. https://doi.org/10.1016/j.colsurfa.2022.128621.

Martínez-Sánchez C, Robles I, Godínez LA (2022) Review of recent developments in electrochemical advanced oxidation processes: application to remove dyes,

709 pharmaceuticals, and pesticides. Int J Environ Sci Technol 19:12611–12678.
710 https://doi.org/10.1007/s13762-021-03762-9

711 Maurya NS, Mittal AK, Cornel P, Rother E (2006) Biosorption of dyes using dead macro fungi:
712 effect of dye structure, ionic strength and pH. Bioresour technol 97:512-521.
713 https://doi.org/10.1016/j.biortech.2005.02.045

714 Mcyotto F, Wei Q, Macharia DK, Huang M, Shen C, Chow CW (2021) Effect of dye structure
715 on color removal efficiency by coagulation. Chem Eng J 405:126674.
716 https://doi.org/10.1016/j.cej.2020.126674

717 Nagendran V, Goveas LC, Vinayagam R, et al. (2025) Challenges and advances in
718 nanocellulose-based adsorbents for dye removal: mechanisms and future directions.
719 Discov Appl Sci 7:14. https://doi.org/10.1007/s42452-024-06413-z

720 Nasuha N, Hameed BH, Din AT (2010) Rejected tea as a potential low-cost adsorbent for the
721 removal of methylene blue. J Hazard Mater 175:126-132.
722 https://doi.org/10.1016/j.jhazmat.2009.09.138

723 Negi A (2025) Cationized cellulose materials: enhancing surface adsorption properties towards
724 synthetic and natural dyes. Polymers 17:36. https://doi.org/10.3390/polym17010036

725 Park S, Baker JO, Himmel ME et al. (2010) Cellulose crystallinity index: measurement
726 techniques and their impact on interpreting cellulase performance. Biotechnol Biofuels
727 3:10. http://doi.org/10.1186/1754-6834-3-10

728 Rahmoun HB, Boumediene M, Ghenim AN, Da Silva EF, Labrincha J (2025) Coupling
729 coagulation–flocculation–sedimentation with adsorption on biosorbent (corncob) for
730 the removal of textile dyes from aqueous solutions. Environments 12:201.
731 https://doi.org/10.3390/environments12060201

732 Saad HE, Mahmoud A (2025) Coumarin-modified cellulose as an efficient adsorbent for
733 cationic dye removal from aqueous environments: synthesis, characterization, and
734 adsorption performance. Sci Rep 15:32511. https://doi.org/10.1038/s41598-025-17789-
735 2

736 Sayed NSM, Ahmed ASA, Abdallah MH, et al. (2024) ZnO@activated carbon derived from
737 wood sawdust as adsorbent for removal of methyl red and methyl orange from aqueous
738 solutions. Sci Rep 14:5384. https://doi.org/10.1038/s41598-024-55158-7

739 Sheikh F, Yasmeen F, Rehman R, Abbas A, Ahmed A, Akram M, Al-thagafi ZT (2026)
740 Cutting-edge developments in revolutionizing chemical technologies using hybrid
741 trends in modern and solar powered wastewater treatment plants for conservation of
742 water resources. Phys Chem Earth 143:104355.
743 https://doi.org/10.1016/j.pce.2026.104355

744 Singh PK, Kumar U, Kumar I, et al. (2024) Critical review on toxic contaminants in surface
745 water ecosystem: sources, monitoring, and its impact on human health. Environ Sci
746 Pollut Res 31:56428–56462. https://doi.org/10.1007/s11356-024-34932-0

747 Stanciu MC, Tanasă F, Teacă CA (2025) Crystallinity changes in modified cellulose substrates
748 evidenced by spectral and X-ray diffraction data. Polysaccharides 6(2):30.
749 http://doi.org/10.3390/polysaccharides6020030

750 Tang Y, Lin T, Jiang C, Zhao Y, Ai S (2021) Renewable adsorbents from carboxylate-modified
751 agro-forestry residues for efficient removal of methylene blue dye. J Phys Chem Solids
752 149:109811. https://doi.org/10.1016/j.jpcs.2020.109811

753 Toprakçürümez H, Recepoğlu YK, Arar Ö (2025) Quaternary ammonium-modified cellulose:
754 a sustainable strategy for purifying aqueous solutions contaminated with sunset yellow
755 dye. Int J Biol Macromol 294:139555. https://doi.org/10.1016/j.ijbiomac.2025.139555

756 Wan H, Zhu X, Wang J, Cao F, Zhang Y, Yao Z, Wang S, Bhattacharyya D, Tang K (2025)
757 Adsorptive nanofibrous membranes for bidirectional removal of cationic and anionic
758 dyes. Sep Purif Technol 361:131515. https://doi.org/10.1016/j.seppur.2025.131515

759 Wang, Y., Xu, L., Li, J et al. (2024) Synthesis of magnetic chitosan-composite biochar and its
760 removal of copper ions (Cu^{2+}) and methylene blue (MB) dye from aqueous solutions.
761 Environ Sci Pollut Res 31:59866–59881. https://doi.org/10.1007/s11356-024-35145-1

762 Wu R, Sun H, Huang P, Su H, Cui H, Wei L, Liu N, Shao G (2026) Hydrogel membrane based
763 on carboxylated lignin-containing cellulose nanofibrils derived from corn stalk through
764 concentrated malic acid pretreatment for dye wastewater purification. Int J Biol
765 Macromol 350:150971. https://doi.org/10.1016/j.ijbiomac.2026.150971

766 Yadav M, Singh N, Annu, Khan SA, Raorane CJ, Shin DK (2024) Recent advances in utilizing
767 lignocellulosic biomass materials as adsorbents for textile dye removal: a
768 comprehensive review. Polymers 16:2417. https://doi.org/10.3390/polym16172417

769 Yang H, Yan R, Chen H et al. (2007) Characteristics of hemicellulose, cellulose and lignin
770 pyrolysis. Fuel 86:1781–1788. https://doi.org/10.1016/j.fuel.2006.12.013

771 Yaseen DA, Scholz M (2019) Textile dye wastewater characteristics and constituents of
772 synthetic effluents: a critical review. Int J Environ Sci Technol 16:1193–1226.
773 https://doi.org/10.1007/s13762-018-2130-z

774 Zhu C, Mahmood Z, Siddique MS, Wang H, Anqi H, Sillanpää M (2021) Structure-based
775 long-term biodegradation of the azo dye: insights from the bacterial community
776 succession and efficiency comparison. Water 13:3017.
777 https://doi.org/10.3390/w13213017

778 Ziembowicz S, Kida M (2025) The optimization of advanced oxidation processes for the
779 degradation of industrial pollutants. Sustainability 17:1908.
780 https://doi.org/10.3390/su17051908
781

782

Supplementary Files

This is a list of supplementary files associated with this preprint. Click to download.

- SupplementaryData.pdf